

Stochastic Long-term Video Interpolation

Qiangeng Xu

qiangenx@usc.edu
University of Southern California

Hanwang Zhang

hanwangzhang@ntu.edu.sg
Nanyang Technological University

Weiyue Wang

weiyuewa@usc.edu
University of Southern California

Peter N. Belhumeur

belhumeur@cs.columbia.edu.com
Columbia University

Ulrich Neumann

uneumann@usc.edu
University of Southern California

Abstract

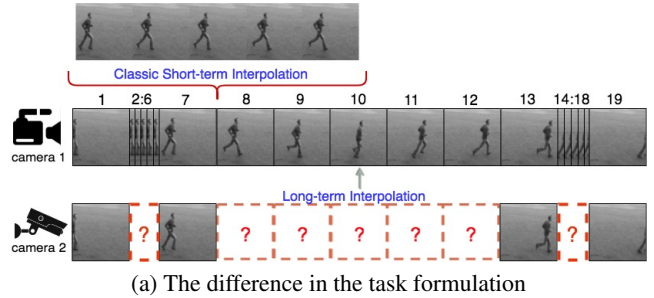
In this paper, we introduce a stochastic learning framework for long-term video interpolation. While most existing interpolation models require two reference frames with a short interval, our framework predicts a plausible intermediate sequence between a long interval. Our model consists of two parts: (1) a deterministic estimation to guarantee the spatial and temporal coherency among frames, (2) a stochastic sampling process to generate dynamics from inferred distributions. Experimental results show that our model is able to generate sharp and clear sequences with variations. Moreover, motions in the generated sequence are realistic and able to transfer smoothly from the referenced start frame to the end frame.

Introduction

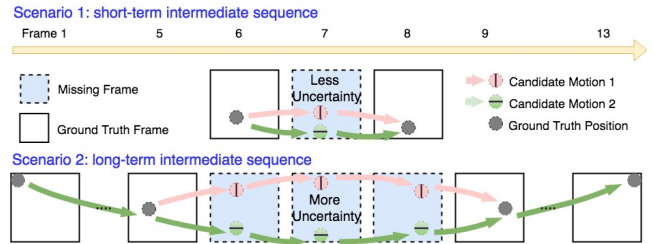
Video interpolation focuses on generating intermediate frames between two reference frames. It is generally applied to the tasks of temporal super-resolution and novel view interpolation. Most studies (Meyer et al. 2018; Jiang et al. 2017) focus on short-term interpolation, aiming to generate in-between frames for videos with original frame rate above 20 fps. Instead, our study focuses on long-term interval inference for videos with frame rate under 3 fps. The applications include missing frames repair, motion planning and especially the temporal quality enhancement for low frame rate security camera and surveillance devices with limited bandwidth. As shown in Figure 1(a), conditioning on the frame 7 and 8, the short-term interpolation generates an intermediate sequence containing similar content. However, the task of long-term interpolation requires to infer varying content and dynamic motions for a long interval (from the frame 8 to 12).

Figure 1(b) illustrates the stochastic nature of the long-term intermediate sequence. We observe the following two phenomena: (1) Compare to the scenario 1, since both the interval length and the difference between the two reference frames are larger, the uncertainties in the long-term intermediate sequence is greater. Therefore, the long-term interpolation has more stochasticity; (2) Taken the frame 5 and 9 as references, both candidate motions in sequence 6:8 are possible. If we also add the frame 1 and 13 as references,

Copyright © 2019, Association for the Advancement of Artificial Intelligence (www.aaai.org). All rights reserved.



(a) The difference in the task formulation



(b) The difference in the level of the stochasticity

Figure 1: (a) A normal camera 1 captures a frame sequence 1 to 19. Short-term interpolation aims to generate 5 frames between the frame 7 to 8. Another low frame rate camera 2 can only capture the frame 1, 7, 13 and 19 of the camera 1. The long-term interpolation task focus on generating the intermediate sequence 8 to 12 for camera 2.

(b) The camera in the scenario 1 can capture every other frame and the camera in the scenario 2 captures 1 frame for every 4 frames. The red and the green trajectories indicate two possible candidate motions in each scenario.

only the candidate motion 2 (the green trajectory) is plausible. Consequently, utilizing long-term information can benefit the dynamic inference by eliminating uncertainties.

Most video interpolation methods (Niklaus and Liu 2018; Liu et al. 2017) rely on estimating the short-term pixel level change. While this approach would fall short of long-term frame synthesis, recent video prediction models (Wichers et al. 2018; Denton and Fergus 2018) can generate frames into the long-term future with explicit motion modeling. In this paper, we model the motion in the same manner as the video prediction. The task has two major challenges: 1.

Unlike the video prediction, the temporal layout of our input is bi-directional and discontinuous. No existing model is applicable; 2. Interpolation requires coherency between the generated sequence and reference frames from both directions. To solve these challenges, we introduce a module **RBCovLSTM**. The *RBCovLSTM* is a multi-layer bi-directional ConvLSTM with residual connections between adjacent layers. To solve the long-term interpolation in 1(a), we input the dynamic features both from the past (frame 1 and 7) and the future (frame 13 and 19) to the *RBCovLSTM*. Each bi-directional layer takes the output from the previous level. Along with the residuals, the dynamic from both sides is gradually propagate to the middle steps. The last layer of *RBCovLSTM* provides reference features to guide the dynamic inference. These reference features play significant roles to enforce the coherency between generated sequence and the reference frames.

The stochastic sampling mechanism (Babaeizadeh et al. 2017) can eliminate the confusion when the network is facing multiple choices. To model the stochasticity in the sequence dynamic, we propose a stochastic learning framework. We first take the two reference frames and the extended reference frames to extract the dynamic features. Then we use the *RBCovLSTM* to create reference features. Every step, a distribution is inferred conditioning on the previous frames and a reference feature. Then we sample a dynamic vector from this distribution for this step. Combining the dynamic vector with previous frames, we can synthesize a new frame in each step. We design our objective function by optimizing a variational lower bound. Our final model can interpolate a sequence for an interval of 9 frames in an RGB real-world video (See Section 1 of the video web page in the supplemental material). To summarize, our contributions are:

- A stochastic model is proposed to generate long-term intermediate sequences. To the best of our knowledge, it is the first stochastic approach to solve interpolation task, and the first model explicitly utilizes the reference frames away from the interval.
- A module *RBCovLSTM* is introduced to solve incoherence in long-term interpolation.
- A movement weight mask in pixel loss is applied to help generate dynamics against the stale content.
- A novel metric is proposed to evaluate the sequence coherency. Experimental results show that our model stands out among previous frameworks on various standard datasets.

Related Works

Most studies of video interpolation (Ilg et al. 2017; Jiang et al. 2017) focus on generating high-quality intermediate frames in a short-term interval. Since we focus on long-term sequence inference, our framework adopts long-term dynamic modeling. Therefore we also refer to the studies of video prediction which have explored this area from various perspectives.

Video Interpolation

Video interpolation generally has three approaches: optical flow based interpolation, phase-based interpolation and deep motion pixels transformation. Optical flow based methods (Herbst, Seitz, and Baker 2009; Yu et al. 2013; Ilg et al. 2017) require an accurate optical flow inference. However, the optical flow estimation is known to be inaccurate for a long time interval. Estimation of the motion dynamic becomes a more favorable option. The phase-based methods such as (Meyer et al. 2015) modify the pixel phase to generate intermediate frames. Although the strategy of propagating phase information is elegant, the high-frequency and drastic changes cannot be properly handled. The inter-frame change will be more significant in our long-term setting. Currently studies (Liu et al. 2017; Niklaus, Mai, and Liu 2017b; Jiang et al. 2017) use deep learning methods to infer the motion flows between the two frames. By far, this branch of approaches achieves the best result and has more potential to solve our task. In our evaluation process, we use SepConv proposed in (Niklaus, Mai, and Liu 2017a) as a comparison.

Deterministic Video Prediction

The mainstream video prediction methods take short consecutive sequences as input and generate deterministic futures by iteratively predicting next frame. (Vondrick, Pirsavash, and Torralba 2016; Mathieu, Couprie, and LeCun 2015) use convolutional network to directly generate each pixel of the new frame. Studies such as (Srivastava, Mansimov, and Salakhudinov 2015; Finn, Goodfellow, and Levine 2016) use a recurrent network to model the dynamic changes and improve the result drastically. (Xingjian et al. 2015) introduces a novel RNN, the ConvLSTM, which has been proved to be powerful in spatial sequence modeling. (Villegas et al. 2017; Denton and others 2017) propose to model the content and the dynamic independently to reduce the workload for the networks. (Tulyakov et al. 2017; Villegas et al. 2017) incorporate GANs (Goodfellow et al. 2014) into their model and improve the generation quality. Notably, two of the generative models (Lu, Hirsch, and Schölkopf 2017) and (Cai et al. 2017) can also conduct long-term interpolation. However both methods, due to their forward generation mechanism, cannot hold the coherency between the last frame and the generated sequence. Our model adopts the decomposition of the motion and the content, uses the ConvLSTM in the motion inference and iteratively generates the frame. However, we don't use GANs since our study focuses more on dynamic inference. We also compare our model with FSTN in (Lu, Hirsch, and Schölkopf 2017), a prediction model that can also handle interpolation tasks.

Stochastic Video Generation

After (Babaeizadeh et al. 2017; Henaff, Zhao, and LeCun 2017) shows the importance of the stochasticity in video prediction, later studies such as (Lee et al. 2018; Denton and Fergus 2018) also conduct the prediction in the form of stochastic sampling. The stochastic prediction process consists of a deterministic distribution inference and a dynamic vector sampling. We also adopt this general procedure. Since SVG-LP introduced in (Denton and Fergus)

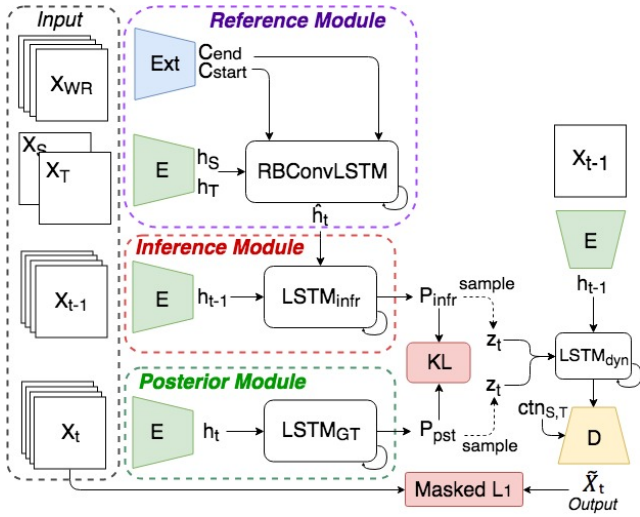


Figure 2: Training: All green *Encoder* module share the same weight. The blue module denotes the *Extractor* and the yellow module denotes the *Decoder*. The Inference module and the Posterior module will produce different z_t and therefore different output frames \tilde{X}_t^{infr} and \tilde{X}_t^{pst} .

is one of the state-of-the-art models and very related to our study, we use the SVG-LP to compare with our model.

Methods

Under the input setting of temporal super-resolution, we formulate our task as follows: For a sequence \mathbf{X} , the camera can only capture one frame out of every u frames. Our study focus on interpolating the sequence $X_{S+1:T-1}$ between adjacent reference frames X_S and X_T . In Figure 1(a), the X_S and X_T are the frame 7 and 13. $X_{S+1:T-1}$ is the sequence from the frame 8 to 12. We also use extended frames (the frame 1 and 19) as additional references.

$$\underbrace{X_{S-e \times u}, \dots, X_{S-u}}_{\text{extended reference frames}}, \underbrace{X_S, X_{S+1:T-1}}_{\text{our target}}, \underbrace{X_T, X_{T+u}, \dots, X_{T+e \times u}}_{\text{extended reference frames}}$$

Here we define a reference frame set: "window of reference" \mathbf{X}_{WR} , which consists of X_S , X_T and the extended reference frames. The hyper parameter e denotes how many extended ground truth frames in each side are included as the references. We will show the impact of these extended information in the ablation study. Although the $P(X_{S+1:T-1} | \mathbf{X}_{WR})$ is better constraint than the $P(X_{S+1:T-1} | X_S, X_T)$, we cannot include as many reference frames as possible. In practice, frames too far away from the target sequence might be unrelated. The redundancy they bring in would hamper the dynamic inference. In the end, we denote the the generated sequence as $\tilde{X}_{S+1:T-1}$.

Like many of the video prediction models (Villegas et al. 2017; Tulyakov et al. 2017), the *Encoder* decomposes each input frame into two representations: a motion dynamic feature $h_t = Enc(X_t)_{dyn}$ and a content residue $ctn_t = Enc(X_t)_{ctn}$. As illustrated in Figure 2, our model consists of 3 major modules.

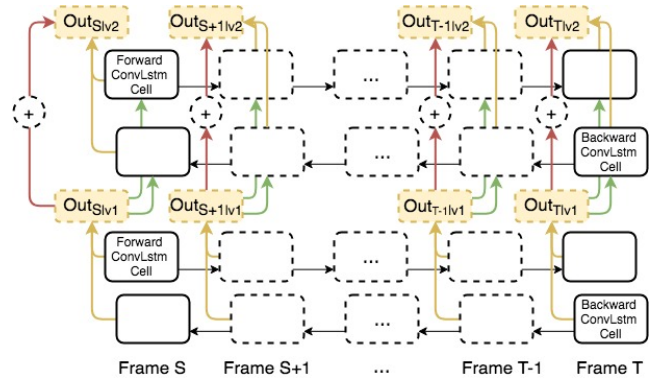


Figure 3: A two layers RBConvLSTM: each layer's output is combined with the residuals from the previous layer.

Reference Module

The reference module includes the *Extractor* and the *RBConvLSTM*, a residual bi-directional ConvLSTM. Based on all the reference frames in \mathbf{X}_{WR} , the *Extractor* learns the momentum and output two vectors C_{start} and C_{end} . The *RBConvLSTM* would use C_{start} as the initial state of its forward cell and C_{end} for its backward cell. For each step t , *RBConvLSTM* outputs a reference hidden vector \hat{h}_t . The whole reference hidden sequence has a conditional distribution $P(\hat{h}_{S:T} | \mathbf{X}_{WR})$.

RBConvLSTM Our reference module is essentially doing a sequence completion. Here we need to transfer an incomplete sequence $h_S, \mathbf{0}, \dots, \mathbf{0}, h_T$ to a complete sequence $\hat{h}_S, \hat{h}_{S+1}, \dots, \hat{h}_{T-1}, \hat{h}_T$. Stacking multiple layers of RNN is a common practice for such task. In our model, features on the bottom layer $h_S, \mathbf{0}, \dots, \mathbf{0}, h_T$ share the same space with the features $\hat{h}_{S:T}$ on the top layer. Therefore, inspired by (He et al. 2015), we decide to add an residual connection between each two layers to elevate the bottom features directly to the top. In the end, RBConvLSTM combines all the three structures: the ConvLSTM, the bi-directional RNN and the residual connections. Its structural details are shown in Figure 3.

Inference Module

We extract a hidden vector h_t from each ground truth frame X_t . On time step t , the *LSTM_infr* takes the h_{t-1} and the reference vector \hat{h}_t , then infers a distribution $P_{infr}(z_t | X_{S:t-1}, \mathbf{X}_{WR})$ for the dynamic changes. This module resembles the prior distribution learning of stochastic prediction methods since the hidden vector h_t is not exposed to the network on step t . Because we also refer to the \hat{h}_t which is conditioning on the \mathbf{X}_{WR} , our distribution now becomes $P_{infr}(z_t | X_{S:t-1}, \mathbf{X}_{WR})$.

Posterior Module

A generated sequence $\tilde{X}_{S+1:T-1}$ can still be valid even it shows different movements than the ground truth. To penalize $\tilde{X}_{S+1:T-1}$ on the target ground truth sequence

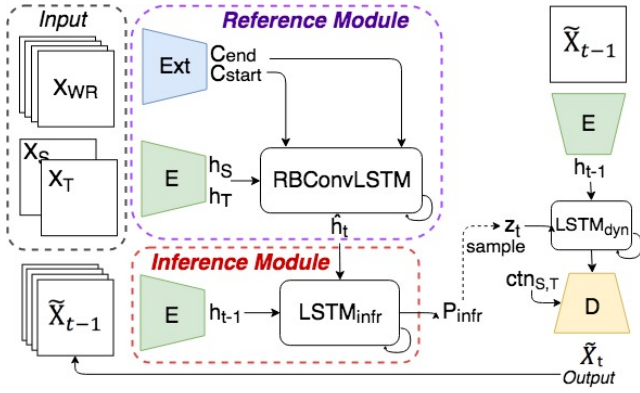


Figure 4: Inference: Without ground truth frame X_{t-1} , the generated frame \tilde{X}_{t-1} serves as the input to the inference module on step t .

$X_{S+1:T-1}$, our model need a mechanism to constrain the dynamic. Similar to stochastic prediction models, our posterior module is exposed to the target frame in each step. The h_t will leak the information to the $LSTM_{GT}$ so it can generate a posterior distribution $P_{pst}(z_t|X_{S:t})$ constraint by the exposed ground truth movement.

Training

After getting $P_{pst}(z_t|X_{S:t})$, we sample a vector z_t^{pst} and concatenate it with h_{t-1} , then, send them into the $LSTM_{dyn}$ to get the motion representation. Along with content residual ctn_S and ctn_T , the Decoder will generate the \tilde{X}_t^{pst} as $Dec(LSTM_{Dym}(h_{S:t}), ctn_S, ctn_T)$. Separately, we would also sample a vector z_t^{infr} from $P_{infr}(z_t|X_{S:t-1}, \mathbf{X}_{WR})$, then use a copy of the $LSTM_{Dym}$ to generate the \tilde{X}_t^{infr} . The training workflow is shown in Figure 2.

Inference

Since the ground truth frames of the target $X_{S+1:T-1}$ are not available during inference, we cannot obtain the X_t at time t . Therefore we only use the inference module to sample the z_t . The inference workflow is shown in Figure 4. Each step, the generated frame \tilde{X}_t will serve as the input for both the $LSTM_{infr}$ and the $LSTM_{Dym}$ in the next step.

Dynamic Spatial Sampling

In order to train P_t^{pst} and P_t^{infr} , we model them as Gaussian distributions $N_{GT}(\mu_t, \sigma_t)$ and $N_{infr}(\mu_t, \sigma_t)$ and use the reparameterization trick from (Kingma and Welling 2013). A Gaussian distribution can be mapped to any distribution through a sufficient complicated function (simulated by a part of our neural network). After inferring the μ_t and the σ_t , we will sample a vector from a normal distribution and calculate the Gaussian. Different from (Denton and Fergus 2018), we consider a spatial vector as a stronger representation for the movement. Different locations in one frame may have different levels of stochasticity. Uniformly draw a sample following the same distribution everywhere will hinder

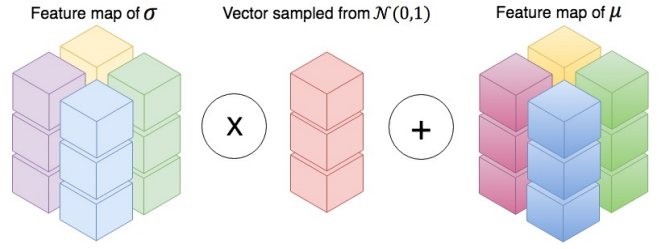


Figure 5: The sampled vector will be applied on all locations.

the modeling. Consequently, we introduce a spatial sampling process (Figure 5). Instead of using 2D vectors, we use two spatial feature maps for μ_t and σ_t . To get the z_t , We multiply the sampled vector on each location of σ_t , then add the μ_t on the product element-wisely.

Loss Function

Because ideally the \tilde{X}_t^{pst} should reconstruct the real X_t , we introduce a pixel loss. Studies such as (Lee et al. 2018) state that although the L_2 loss generally gives better result on SSIM and PSNR, it will produce blurry images. Here we choose to use the $L_1(X_t, \tilde{X}_t^{pst})$. Since we only use the inference module during the testing phase, we need to train $P_{infr}(z_t|X_{S:t-1}, \mathbf{X}_{WR})$ to predict the dynamic change. On the other hand, the $P_{pst}(z_t|X_{S:t})$ has to carry the dynamic change from the h_t to reconstruct the X_t . Therefore here we also add two KL divergences between $P_{infr}(z_t|X_{S:t-1}, \mathbf{X}_{WR})$ and $P_{pst}(z_t|X_{S:t})$. Besides, we observe that directly imposing a pixel loss on the \tilde{X}_t^{infr} after the P_{infr} becomes stable can further improve the video quality. Our final objective is to minimize the combined loss:

$$L_C = \sum_{t=s+1}^{T-1} [\beta \cdot L_1(X_t, \tilde{X}_t^{pst}) + (1 - \beta) \cdot L_1(X_t, \tilde{X}_t^{infr}) + \alpha \cdot D_{KL}(P_{pst}||P_{infr}) + \gamma \cdot D_{KL}(P_{infr}||P_{pst})] \quad (1)$$

The β balances the posterior reconstruction and the inference reconstruction, while the α and the γ determines the trade-off between the reconstruction and the similarity between the two distributions. Both the forward and the reverse KL-divergence of P_{infr} and P_{pst} achieve the minimum when the two distributions are equal. However, according to (Fox and Roberts 2012), since $D_{KL}(P_{pst}||P_{infr})$ is sampled on P_{pst} , it will penalize more when P_{pst} is large and P_{infr} is small. Therefore this term will lead to a P_{infr} with richer diversity. On the other hand, $D_{KL}(P_{infr}||P_{pst})$ will make the inference more accurate when P_{infr} has large value. To better serve our task, we decide to keep both terms to strike a balance between accuracy and diversity. To theoretically validate this loss function, We develop a variational lower bound which is inspired by the ELBO in (Kingma and Welling 2013). To maximize a sequence's probability in the $P(\tilde{X}_{S:T})$. We can maximize the variational lower bound of its logarithm (See Appendix A in the supplemental material for details):

$$\sum_{t=S}^{T-1} \mathbb{E}_{Q(z_t)} \log P(\tilde{X}_t|\tilde{X}_{S:t-1}, z_{S:t}) - \int_z Q(z_{S:T}) \log \frac{Q(z_{S:T})}{P(z_{S:T})} \quad (2)$$

Since we are interested in maximizing $\log P(\tilde{X}_{S:T-1}^{infr})$, we can fit P_{pst} and P_{infr} into (2)'s $P(z_{S:t})$ and $Q(z_{S:t})$:

$$\log P(\tilde{X}_{S:T-1}^{infr}) \geq \sum_{t=S}^{T-1} \left[\mathbb{E}_{P_{infr}(z_t)} \log P(X_t^{infr} | X_{S:t-1}^{infr}, z_{S:t}^{infr}) - D_{KL} \left(P_{infr}(z_t | X_{S:t-1}^{infr}, \mathbf{X}_{WR}) || P_{pst}(z_t | X_{S:t}^{pst}) \right) \right] \quad (3)$$

However, if we only maximize the lower bound above, the $LSTM_{GT}$ will tend to ignore the information in X_t since it has not been exposed to $LSTM_{infr}$ on time step t . The $P_{infr}(z_t)$ and $P_{infr}(z_t)$ will degenerate to a convenient fixed value to lower the D_{KL} . Thus we also need to improve the reconstruction of X_t and maximize $\log P(\tilde{X}_{S:T-1}^{pst})$. Similarly, we fit P_{infr} and P_{pst} into (2)'s $P(z_{S:t})$ and $Q(z_{S:T})$ to get its variational lower bound :

$$\log P(\tilde{X}_{S:T-1}^{pst}) \geq \sum_{t=S}^{T-1} \left[\mathbb{E}_{Q_{pst}(z_t)} \log P(X_t^{pst} | X_{S:t-1}^{pst}, z_{S:t}^{pst}) - D_{KL} \left(Q_{pst}(z_t | X_{S:t-1}^{pst}) || P_{infr}(z_t | X_{S:t-1}^{infr}, \mathbf{X}_{WR}) \right) \right] \quad (4)$$

We can see in the loss function (1): The first loss term is to help increase the first term of (4). The second loss term is aiming to improve the first term of (3). The third and the fourth loss terms would penalize the second terms in (3) and (4). More details of the explanation and deduction can be found in Appendix B in the supplemental material.

Movement Weight Mask We apply a movement weight mask to each location of the pixel loss. If a pixel value stays the same as the previous step, the weight is 1 on that location. Otherwise, we either set the weight to 0 if it's a flickering pixel (determined by its isolation level) or set the weight to $\eta > 1$ to penalize more on the moving region. This operation helps us to (1) denoise the content changes, (2) encourage the dynamic learning to prevent the stale sequence generation. The mask is visualized in Figure 9 and 10.

Experiments

We test our model on three datasets with different dynamics: Stochastic Moving MNIST(SM-MNIST) (Denton and Fergus 2018) for bouncing rule with random momentum, KTH Action Database (Schuldt, Laptev, and Caputo 2004) for deformable objects (human body) and BAIR robot pushing dataset (Ebert et al. 2017) for sudden stochastic movements. A generated sequence that is different from the ground truth (low SSIM and PSNR) can still be valid if its dynamic pattern makes sense. Thus we introduce the last momentum similarity (LMS) calculated by the mean square distance between the optical flow from X_{T-1} to X_T and the optical flow from \tilde{X}_{T-1}^{infr} to X_T . We find LMS a good indicator of the video coherency since no matter how the dynamic being sampled, both the object's position and speed should make a smooth transition to X_T . Three metrics are used for quantitative evaluation: structural similarity (SSIM), Peak Signal-to-Noise Ratio (PSNR), and LMS. We compare our results with other state-of-the-art models: SepConv(Niklaus, Mai,

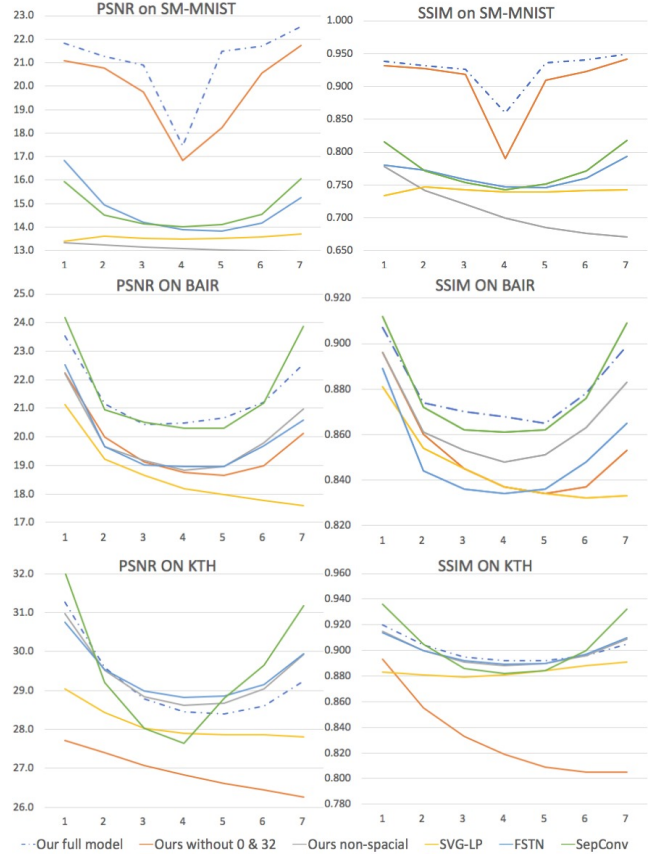


Figure 6: Metrics averaging overall all SM-MNIST's test sequences for each step.

and Liu 2017a), a high-performance interpolation model; FSTN(Lu, Hirsch, and Schölkopf 2017), a deterministic generation model with the capability of interpolation; and SVP(Denton and Fergus 2018), an advanced stochastic prediction model. Since FSTN and SVP are not aiming to solve the long-term interpolation, we further concatenate the representation of the last frame X_T to their dynamic feature maps in each time step. Ablation studies are conducted by removing the spatial sampling or the extensive references in \mathbf{X}_{WR} . Due to SepConv's limitation (can only interpolate sequence with the length of $2^n - 1$), all the following evaluations are under the interpolation of 7 intermediate frames. More video results for various settings (see the video web page), network architectures and the training details (see Appendix C) can be found in the supplementary material.

Stochastic Moving MNIST (SM-MNIST)

Different from the moving MNIST, a digit in SM-MNIST introduced by (Denton and Fergus 2018) will bounce off the wall with a random speed and a random direction. Since the dataset contains no pixel noise and no static content, applying the movement weight mask is unnecessary. Although the dataset only contains non-deformable objects moving in simple patterns, the uncertainties of the outcome after a bounce make it a challenging task for all methods. The Avg

	SM-MNIST			BAIR			KTH		
	Avg PSNR	Avg SSIM	Avg LMS	Avg PSNR	Avg SSIM	Avg LMS	Avg PSNR	Avg SSIM	Avg LMS
Our full model	21.025	0.926	0.303	21.432	0.880	1.05	29.190	0.901	0.248
Ours without 0 & 24	19.857	0.906	0.353	19.694	0.852	1.36	26.907	0.831	0.478
Ours non-spatial	13.207	0.752	6.394	19.938	0.865	1.159	29.366	0.896	0.276
SVG-LP	13.543	0.741	5.393	18.648	0.846	1.891	28.131	0.883	0.539
FSTN	14.730	0.765	3.773	19.908	0.850	1.332	29.431	0.899	0.264
SepConv	14.759	0.775	2.160	21.615	0.877	1.237	29.210	0.904	0.261

Table 1: Result of metrics averaging over all frames. Here we report the score of the best sampled sequence for our model.

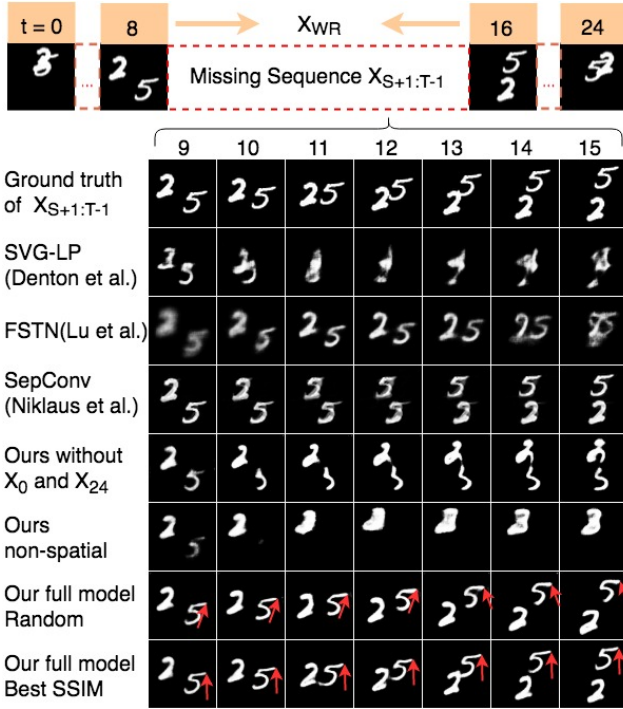


Figure 7: The digit 5 in our best sequence follows the upward trajectory of the ground truth. In our another randomly sampled sequence, the 5 goes upper right and then bounce upper left.

PSNR, SSIM and LMS over all test frames are shown in Table 1. We also plot the metric values averaging over all test sequences on each step in Figure 6. To qualitatively evaluate our methods, here we show an example in Figure 7. when the two digits in frames 8 and 16 having significant position differences, interpolation models such as SepConv would still choose to move the pixel based on the proximity between the two frames. We can see that the digits 2 and 5 gradually transfer to each other since the 2 in the frame 8 is closer to the 5 in the frame 16. Because the deterministic generation model FSTN cannot handle the uncertainties of the speed and the direction after a bounce, the model gets confused and generates a blurry result. The SVG-LP cannot converge in this setting since it doesn't have a planning module like the *RBCConvLSTM* to lead the sequence to the final frame. Without spatial independence, a non-spatial representation cannot sample different dynamics for different

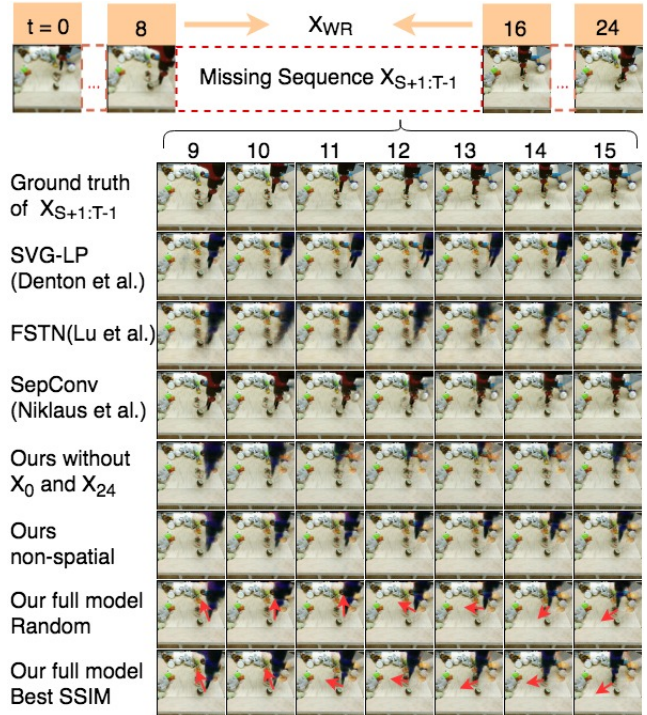


Figure 8: The arm in the best sequence follows the same movements in ground truth: first move upward left then downward left. In another sampled sequence, the arm firstly goes straight up and then straight left, finally downward left.

areas. Although there are 2 moving digits, the two digits in the result of "Ours non-spatial" collapse into one, then move toward the final frame. Finally, our full model can learn the bouncing rule and provide plausible alternative sequences. Although our randomly sampled sequence diverges from the ground truth, this sequence can still keep the coherency with the frame 8 and 16, moving under a reasonable pattern.

BAIR robot pushing dataset

The BAIR robo pushing dataset (Ebert et al. 2017) contains sequences of a robot arm pushing various objects in the RGB domain. The movements of the arm don't follow smooth trajectories, and the movement changes are prompt. As shown in Table 1, although our model marginally outperforms other models on SSIM, the SepConv achieves the best PSNR. As shown in Figure 8, since the SepConv relies more on pixel proximity, the shapes of the static objects in this method are

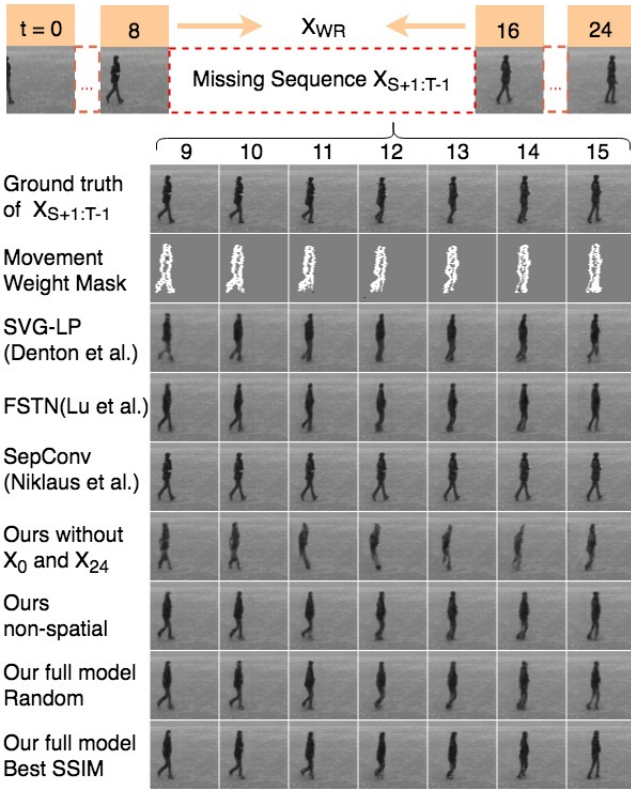


Figure 9: Although the SepConv generates sharp frames, its sliding tendency will cause dynamic errors and high LMS.

nically preserved. However, the result of the SepConv in Figure 8 loses the stochasticity while its movement is simplified to a straight sliding. The frames in the middle suffer the most in all metrics (Figure 6), due to this sliding inclination. The stochasticity of the movement makes it hard for SVG-LP’s arm to go back to the final frame and for FSTN to generate sharp shapes. The objects created by our model without spatial sampling are more blurry, since all the areas will be disturbed by the dynamic change. On the other hand, the result of our model without using the frame 0 and 24 as references diverge too much away from the ground truth movement. Our full model can not only sample a similar sequence to the ground truth, but sequences with reasonably varied movements (Figure 8).

KTH Action Dataset

The KTH Action dataset (Schuldt, Laptev, and Caputo 2004) is a standard video generation dataset containing real-world videos of six human actions. Although the background is uniform, there is still some pixel noise. We found setting the mask’s weight η to 5 on moving pixels and 0 on noise is beneficial. Since most actions in the dataset such as waving follow fix patterns, the FSTN and the SepConv can achieve the best scores in PSNR and SSIM (Table 1). However, if the object in the frame 8 and 16 has a similar body pose, the SepConv will freeze the object’s body and slide the object to its new position (Figure 9). Indicated by the example

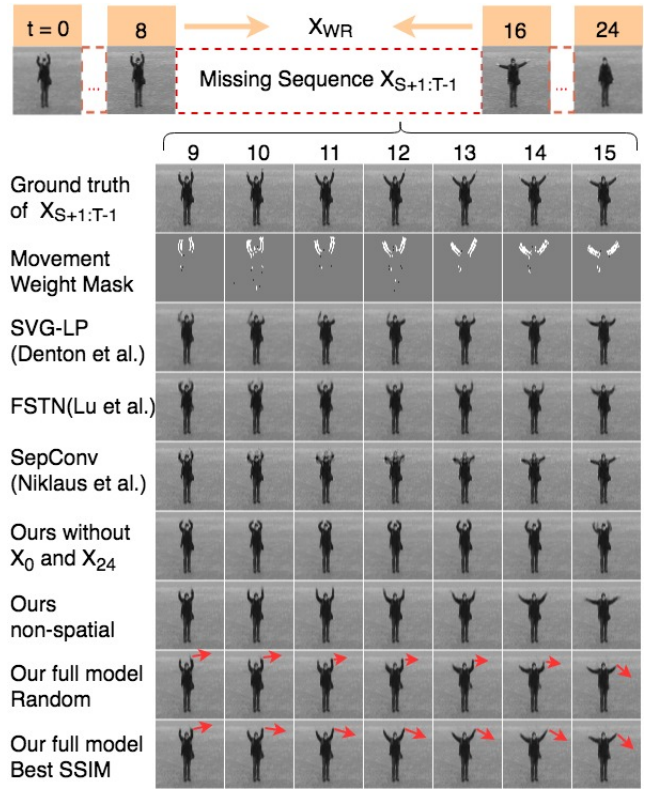


Figure 10: Our best sampled sequence keeps the arm straight. In another randomly sampled sequence, the forearm bends first then stretches straight in the end.

in Figure 10, the result of deterministic method FSTN contains blurry pixels on moving region although it keeps the static parts sharp. Our model without the frame 0 and 24 as references suffers from the uncertainties of the initial state (Figure 9). Our sequence with best SSIM has a similar pattern as the ground truth. Even the random sampled sequence shown in the second last row of Figure 10 has different dynamics in the middle, its initial and final movements still stick to the ground truth. Therefore our model still achieves an outstanding LMS over other methods (Table 1).

Conclusions and Future Work

We have presented a stochastic learning framework that can interpolate intermediate sequences between long-term frame intervals. To the best of our knowledge, it is the first study using extended reference frames for video interpolation. Three modules (the reference module, the inference module and the posterior module) are introduced to sample a plausible sequence that preserves the interpolation consistency and the movement variety. Extensive ablation studies and comparison experiments with state-of-the-art methods demonstrate our good performance on three popular datasets. A new metric LMS is also proposed to evaluate the sequence coherency. The future work will focus on improving the quality of the long-term video interpolation and generating high-resolution sequences.

References

- [Babaeizadeh et al. 2017] Babaeizadeh, M.; Finn, C.; Erhan, D.; Campbell, R. H.; and Levine, S. 2017. Stochastic variational video prediction. *arXiv preprint arXiv:1710.11252*.
- [Cai et al. 2017] Cai, H.; Bai, C.; Tai, Y.-W.; and Tang, C.-K. 2017. Deep video generation, prediction and completion of human action sequences. *arXiv preprint arXiv:1711.08682*.
- [Denton and Fergus 2018] Denton, E., and Fergus, R. 2018. Stochastic video generation with a learned prior. *arXiv preprint arXiv:1802.07687*.
- [Denton and others 2017] Denton, E. L., et al. 2017. Un-supervised learning of disentangled representations from video. In *Advances in Neural Information Processing Systems*, 4414–4423.
- [Ebert et al. 2017] Ebert, F.; Finn, C.; Lee, A. X.; and Levine, S. 2017. Self-supervised visual planning with temporal skip connections. *arXiv preprint arXiv:1710.05268*.
- [Finn, Goodfellow, and Levine 2016] Finn, C.; Goodfellow, I.; and Levine, S. 2016. Unsupervised learning for physical interaction through video prediction. In *Advances in neural information processing systems*, 64–72.
- [Fox and Roberts 2012] Fox, C. W., and Roberts, S. J. 2012. A tutorial on variational bayesian inference. *Artificial intelligence review* 38(2):85–95.
- [Goodfellow et al. 2014] Goodfellow, I.; Pouget-Abadie, J.; Mirza, M.; Xu, B.; Warde-Farley, D.; Ozair, S.; Courville, A.; and Bengio, Y. 2014. Generative adversarial nets. In *Advances in neural information processing systems*, 2672–2680.
- [He et al. 2015] He, K.; Zhang, X.; Ren, S.; and Sun, J. 2015. Deep residual learning for image recognition. corr, vol. abs/1512.03385.
- [Henaff, Zhao, and LeCun 2017] Henaff, M.; Zhao, J.; and LeCun, Y. 2017. Prediction under uncertainty with error-encoding networks. *arXiv preprint arXiv:1711.04994*.
- [Herbst, Seitz, and Baker 2009] Herbst, E.; Seitz, S.; and Baker, S. 2009. Occlusion reasoning for temporal interpolation using optical flow. *Department of Computer Science and Engineering, University of Washington, Tech. Rep. UW-CSE-09-08-01*.
- [Ilg et al. 2017] Ilg, E.; Mayer, N.; Saikia, T.; Keuper, M.; Dosovitskiy, A.; and Brox, T. 2017. FlowNet 2.0: Evolution of optical flow estimation with deep networks. In *IEEE conference on computer vision and pattern recognition (CVPR)*, volume 2, 6.
- [Jiang et al. 2017] Jiang, H.; Sun, D.; Jampani, V.; Yang, M.-H.; Learned-Miller, E.; and Kautz, J. 2017. Super slomo: High quality estimation of multiple intermediate frames for video interpolation. *arXiv preprint arXiv:1712.00080*.
- [Kingma and Welling 2013] Kingma, D. P., and Welling, M. 2013. Auto-encoding variational bayes. *arXiv preprint arXiv:1312.6114*.
- [Lee et al. 2018] Lee, A. X.; Zhang, R.; Ebert, F.; Abbeel, P.; Finn, C.; and Levine, S. 2018. Stochastic adversarial video prediction. *arXiv preprint arXiv:1804.01523*.
- [Liu et al. 2017] Liu, Z.; Yeh, R. A.; Tang, X.; Liu, Y.; and Agarwala, A. 2017. Video frame synthesis using deep voxel flow. In *ICCV*, 4473–4481.
- [Lu, Hirsch, and Schölkopf 2017] Lu, C.; Hirsch, M.; and Schölkopf, B. 2017. Flexible spatio-temporal networks for video prediction. In *Proceedings of the IEEE Conference on Computer Vision and Pattern Recognition*, 6523–6531.
- [Mathieu, Couprie, and LeCun 2015] Mathieu, M.; Couprie, C.; and LeCun, Y. 2015. Deep multi-scale video prediction beyond mean square error. *arXiv preprint arXiv:1511.05440*.
- [Meyer et al. 2015] Meyer, S.; Wang, O.; Zimmer, H.; Grosse, M.; and Sorkine-Hornung, A. 2015. Phase-based frame interpolation for video. In *Proceedings of the IEEE Conference on Computer Vision and Pattern Recognition*, 1410–1418.
- [Meyer et al. 2018] Meyer, S.; Djelouah, A.; McWilliams, B.; Sorkine-Hornung, A.; Gross, M.; and Schroers, C. 2018. Phasenet for video frame interpolation. In *Proceedings of the IEEE Conference on Computer Vision and Pattern Recognition*, 498–507.
- [Niklaus and Liu 2018] Niklaus, S., and Liu, F. 2018. Context-aware synthesis for video frame interpolation. *arXiv preprint arXiv:1803.10967*.
- [Niklaus, Mai, and Liu 2017a] Niklaus, S.; Mai, L.; and Liu, F. 2017a. Video frame interpolation via adaptive convolution. In *IEEE Conference on Computer Vision and Pattern Recognition*, volume 1, 3.
- [Niklaus, Mai, and Liu 2017b] Niklaus, S.; Mai, L.; and Liu, F. 2017b. Video frame interpolation via adaptive separable convolution. *CoRR* abs/1708.01692.
- [Schuldt, Laptev, and Caputo 2004] Schuldt, C.; Laptev, I.; and Caputo, B. 2004. Recognizing human actions: a local svm approach. In *Pattern Recognition, 2004. ICPR 2004. Proceedings of the 17th International Conference on*, volume 3, 32–36. IEEE.
- [Srivastava, Mansimov, and Salakhudinov 2015] Srivastava, N.; Mansimov, E.; and Salakhudinov, R. 2015. Unsupervised learning of video representations using lstms. In *International conference on machine learning*, 843–852.
- [Tulyakov et al. 2017] Tulyakov, S.; Liu, M.-Y.; Yang, X.; and Kautz, J. 2017. Mocogan: Decomposing motion and content for video generation. *arXiv preprint arXiv:1707.04993*.
- [Villegas et al. 2017] Villegas, R.; Yang, J.; Hong, S.; Lin, X.; and Lee, H. 2017. Decomposing motion and content for natural video sequence prediction. *arXiv preprint arXiv:1706.08033*.
- [Vondrick, Pirsivash, and Torralba 2016] Vondrick, C.; Pirsivash, H.; and Torralba, A. 2016. Generating videos with scene dynamics. In *Advances In Neural Information Processing Systems*, 613–621.
- [Wichers et al. 2018] Wichers, N.; Villegas, R.; Erhan, D.; and Lee, H. 2018. Hierarchical long-term video prediction without supervision. *arXiv preprint arXiv:1806.04768*.

[Xingjian et al. 2015] Xingjian, S.; Chen, Z.; Wang, H.; Yeung, D.-Y.; Wong, W.-K.; and Woo, W.-c. 2015. Convolutional lstm network: A machine learning approach for precipitation nowcasting. In *Advances in neural information processing systems*, 802–810.

[Yu et al. 2013] Yu, Z.; Li, H.; Wang, Z.; Hu, Z.; and Chen, C. W. 2013. Multi-level video frame interpolation: Exploiting the interaction among different levels. *IEEE Transactions on Circuits and Systems for Video Technology* 23(7):1235–1248.

Appendices

Appendix A. Proof of the Variational Lower Bound

We can set $P(\tilde{X}_{S:T})$ as the probability of any sequence. The logarithm of this probability has the following variational lower bound:

$$\log P(\tilde{X}_{S+1:T-1}) = \log \int_z P(\tilde{X}_{S+1:T-1}|z_{S:T-1})P(z_{S:T-1})\frac{Q(z_{S:T})}{Q(z_{S:T})} \quad (5)$$

$$= \log \mathbb{E}_{Q(z_{S:T})} \frac{P(\tilde{X}_{S+1:T-1}|z_{S:T-1})P(z_{S:T})}{Q(z_{S:T})} \quad (6)$$

$$\geq \mathbb{E}_{Q(z_{S:T})} \frac{P(\tilde{X}_{S+1:T-1}|z_{S:T-1})P(z_{S:T})}{Q(z_{S:T})} \quad (7)$$

$$= \mathbb{E}_{Q(z_{S:T})} \log P(\tilde{X}_{S+1:T-1}|z_{S:T-1}) - E_{Q(z_{S:T})} \frac{Q(z_{S:T})}{P(z_{S:T})} \quad (8)$$

$$= \mathbb{E}_{Q(z_{S:T})} \log \prod_t P(\tilde{X}_t|\tilde{X}_{S:t-1}, z_{S:t}) - \int_z Q(z_{S:T}) \log \frac{Q(z_{S:T})}{P(z_{S:T})} \quad (9)$$

$$= \sum_{t=S}^{T-1} \mathbb{E}_{Q(z_t)} \log P(\tilde{X}_t|\tilde{X}_{S:t-1}, z_{S:t}) - \int_z Q(z_{S:T}) \log \frac{Q(z_{S:T})}{P(z_{S:T})} \quad (10)$$

Appendix B. Explanation of the Deduction and the Reasoning

Since we use the output from the inference section as the result during inference phase, we are mostly interested in maximizing $\log P(\tilde{X}_{S:T-1}^{infr})$. Since the lower bound shown in Appendix A will hold for any form of the distribution, we can fit P_{pst} and P_{infr} into (10)'s $P(z_{S:t})$ and $Q(z_{S:T})$:

$$\log P(\tilde{X}_{S:T-1}^{infr}) \geq \sum_{t=S}^{T-1} \left[\mathbb{E}_{P_{infr}(z_t)} \log P(X_t^{infr}|X_{S:t-1}^{infr}, z_{S:t}^{infr}) - \int_{z_{S:T-1}^{infr}} P_{infr} \cdot \log \frac{P_{infr}}{P_{pst}} \right] \quad (11)$$

The integration part (KL divergence of the sequence) in the above inequality can be decomposed as:

$$\int_{z_{S:T-1}^{infr}} P_{infr} \cdot \log \frac{P_{infr}}{P_{pst}} = \int_{z_S^{infr}} \int_{z_{S+1}^{infr}} \cdots \int_{z_{T-1}^{infr}} \left[\prod_{t=S}^T P_{infr}(z_t|X_{S:t-1}^{infr}, X_{WR}) \cdot \sum_t \log \frac{P_{infr}(z_t|X_{S:t-1}^{infr}, X_{WR})}{P_{pst}(z_t|X_{S:t}^{pst})} \right] \quad (12)$$

$$= \sum_{t=1}^{T-1} \mathbb{E}_{P_{infr}(z_t|X_{S:t-1}^{infr}, X_{WR})} \log \frac{P_{infr}(z_t|X_{S:t-1}^{infr}, X_{WR})}{P_{pst}(z_t|X_{S:t}^{pst})} \quad (13)$$

$$= \sum_{t=1}^{T-1} D_{KL}(P_{infr}(z_t|X_{S:t-1}^{infr}, X_{WR})||P_{pst}(z_t|X_{S:t}^{pst})) \quad (14)$$

Therefore if we put (14) back to the lower bound (11), the logarithm of the probability we want to maximize becomes:

$$\log P(\tilde{X}_{S:T-1}^{infr}) = \sum_{t=S}^{T-1} \left[\mathbb{E}_{P_{infr}(z_t)} \log P(X_t^{infr}|X_{S:t-1}^{infr}, z_{S:t}^{infr}) - D_{KL}(P_{infr}(z_t|X_{S:t-1}^{infr}, X_{WR})||P_{pst}(z_t|X_{S:t}^{pst})) \right] \quad (15)$$

Because the neural network sometimes has the tendency to use the easiest way to fit the objective, if we only maximize (15), the $LSTM_{GT}$ will ignore the information introduced by X_t . The $P_{infr}(z_t)$ and $P_{infr}(z_t)$ will degenerate to a convenient fixed value to lower the D_{KL} . Our inference module and posterior module then will resembles the SVG-FP, which is a simpler version of SVG-LP with fixed prior distribution.

To prevent the degeneration, we also need to maximize the probability of the reconstruction result \tilde{X}_t^{pst} to force the newly observed dynamic from X_t to be included in P_{pst} . Here we fit P_{infr} and P_{pst} into (10)'s $P(z_{S:t})$ and $Q(z_{S:t})$ and we end up also maximizing:

$$\log P(\tilde{X}_{S:T-1}^{pst}) = \sum_{t=S}^{T-1} \left[\mathbb{E}_{P_{pst}(z_t)} \log P(X_t^{pst}|X_{S:t-1}^{pst}, z_{S:t}^{pst}) - D_{KL}(P_{pst}(z_t|X_{S:t-1}^{pst})||P_{infr}(z_t|X_{S:t-1}^{infr}, X_{WR})) \right] \quad (16)$$

The deduction process of this result is the same as the transformation from (11) to (15). Finally, we design a objective function to maximize both of (15) and (16) at the same time.

Appendix C. Architecture and Training Details

The *Encoder*, the *Extractor* and the *Decoder* use the same architecture of DCGAN. For step S and T , feature maps of all layers in *Encoder* will be gathered as a multi-scale residuals ctn_S and ctn_T to help reconstruct the static content. The $LSTM_{infr}$, the $LSTM_{pst}$ and the $LSTM_{dyn}$

Feature	Dimension 1	Dimension 2	Dimension 3
C_{start}	4	4	256
C_{end}	4	4	256
h_t	4	4	256
\hat{h}_t	4	4	256
σ_t SMMNIST & KTH	4	4	32
μ_t SMMNIST & KTH	4	4	32
σ_t BAIR	4	4	64
μ_t BAIR	4	4	64

Table 2: Dimensionality of different features

Training Parameters	SMMNIST	BAIR	KTH
α	0.002	0.0002	0.0002
γ	0.001	0.0001	0.0001
β	1 to 0.4	1 to 0.4	1 to 0.4
Mask Weight η	N/A	2	5

Table 3: Hyper parameters for training on different datasets

use the structure of one layer ConvLSTM. The output dimensions of our modules are listed in Table 2.

For the evaluation presented in our paper, all datasets have been trained with a input frame dimension of 64×64 with a interval of 7 frames. We also train on KTH with a input frame dimension of 128×128 (See Section 2 in the video web page) and BAIR with intervals of 9 frames (See Section 1 in the video web page). We use standard Adam optimizer with 0.5 as the first momentum decay rate. All settings of the hyper parameters for different datasets are shown in 3. The β is initially set to 1 and gradually reduce to 0.4. To prevent the accumulation of errors, we will first roll back the cell state of $LSTM_{in,fr}$ to $t - 1$, and then input h_t after inferring the $N_{in,fr}(\mu_t, \sigma_t)$. This operation has been proved to be crucial to our result. On the early stage of the training, a less meaningful \hat{h}_t would accumulatively disturb the cell state of $LSTM_{in,fr}$ and lead to a slow convergence.